

Fig. 5—Fractograph of a tension-tested specimen.

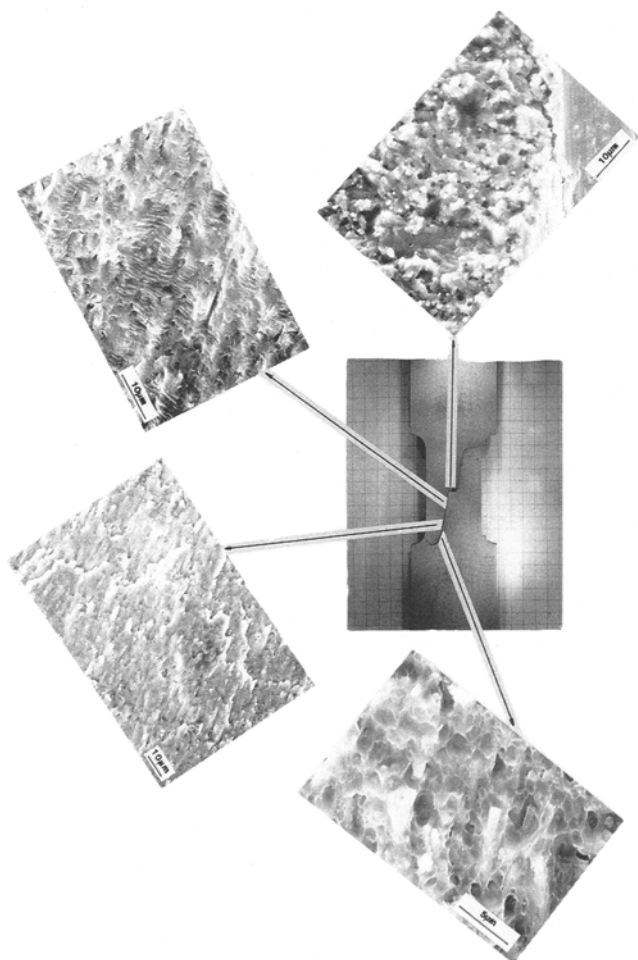


Fig. 6—Fractographs of a fatigue-fractured specimen.

fewer striations are visible. After the transverse deflection of the crack path, only white dots (transverse section images of SiC whiskers) and dimples are seen.

It has been known that in the period of stable fatigue crack growth, the maximum stress intensity factor K_{\max} is less than the critical stress intensity factor K_c , i.e., $K_{\max} < K_c$. On the other hand, during the tensile fracture or the overload fracture following the stable fatigue crack growth, $K_{\max} \geq K_c$. Taking this into account, the results of this study can be summarized as follows.

- (1) The SiC whiskers are aligned in the extrusion direction.
- (2) During stable fatigue crack growth under loading with $K_{\max} < K_c$, the crack growth path is nearly parallel to or along the longitudinal interface of the aligned SiC whiskers. In this stage, fatigue striations are developed on a longitudinal matrix crack plane.
- (3) During the tensile fracture or the overload fracture following stable fatigue crack growth under loading with $K_{\max} \geq K_c$, the crack path is transverse to the aligned SiC whiskers. In this stage, dimples are formed in the matrix.

Extended Al(Mn) Solution in a Rapidly Solidified Al-Li-Mn-Zr Alloy

M. RUHR, E.J. LAVERNIA, and J.C. BARAM

In the present communication, the effect of cooling rate on the extension of Mn solid solubility in Al and on the relative amount of MnAl (MnAl_6 and MnAl_4) secondary phases during gas atomization and spray deposition is critically examined.^[1,2] An alloy of composition Al-6.5Mn-2.3Li-0.65Zr (wt pct) currently being investigated for applications requiring high strength and low density at high temperatures was selected for this study. The material was exposed to various solidification histories by altering gas pressure and powder size during solidification. The resulting six distinct cooling rates were characterized for the following samples (labeled A through F):

- (1) Sample A consisted of high pressure argon gas atomized powders sieved in the $<45 \mu\text{m}$ size fraction, all spherical in shape. Particle size analysis (by sedimentation) showed that about 60 wt pct of that size fraction consisted of powders 10 to 20 μm in diameter. The argon gas pressure used for atomization was 50 atm.
- (2) Sample B consisted of powders processed identically to those used in sample A but sieved in the +125/-150 μm size fraction. These powders were mostly spherical.
- (3) Sample C was made up of overspray fine powders

M. RUHR, Graduate Student, and J.C. BARAM, Associate Professor, are with the Materials Engineering Department, Ben-Gurion University of the Negev, Beer-Sheva, Israel. E.J. LAVERNIA, Assistant Professor, is with the Materials Section, Mechanical Engineering Department, Materials Section, University of California at Irvine, Irvine, CA 92717.

Manuscript submitted December 12, 1988.

(sieved in the $<53\text{ }\mu\text{m}$ size fraction) collected after a spray atomization and deposition experiment. Particle size analysis (by sedimentation) showed that about 60 wt pct of that size fraction was comprised of 20 to 30 μm powders. The spherical shape of the powders is an indication that the solidification occurred in flight. The gas pressure used in this experiment was 17 atm.

(4) Sample D consisted of powders processed identically to those used in sample C but in the $+125/-150\text{ }\mu\text{m}$ size fraction. These powders appeared to have a flat, elongated, nonspherical shape. This is an indication that solidification of the powders from sample D did not take place in flight but after impacting the atomization chamber walls.

(5) Samples E and F were obtained from spray atomized and deposited compacts and, hence, unlike samples A through D were not discrete powders. In this experiment, argon gas at 17 atm gas pressure was used to atomize a molten stream of metal and direct the resulting distribution of droplets against a water-cooled copper quenching substrate where they impacted and built into a compact. The material was deposited in a disklike shape, approximately 15 cm in diameter and 6 cm in height. Samples E and F correspond to the top and bottom 3 cm, respectively, of the compact center region. More details on spray atomization and deposition are presented elsewhere.^[1,2,3] The morphology of the various samples is shown in Figure 1.

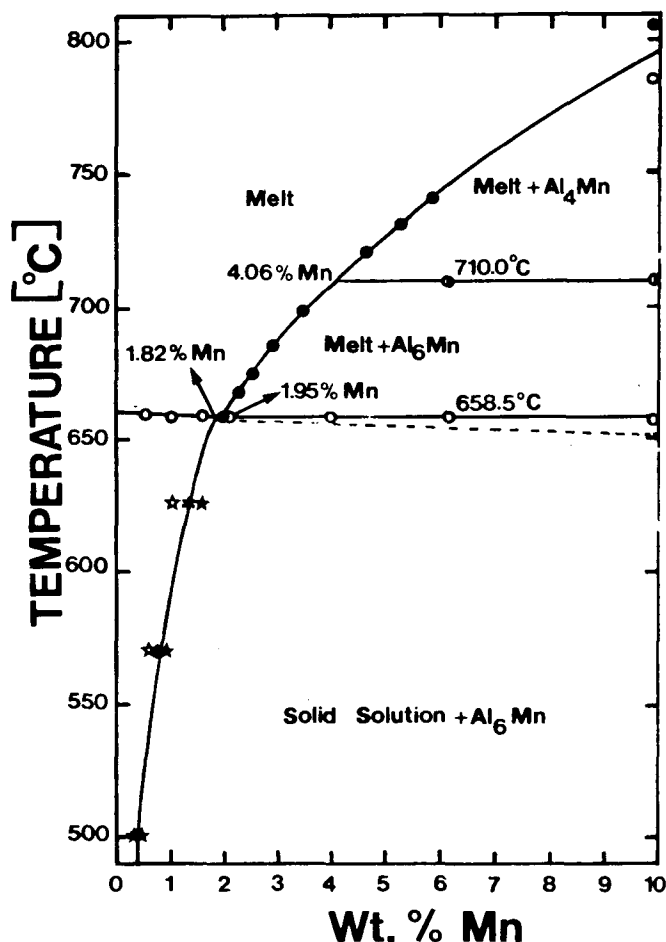


Fig. 1—Morphology of samples A through F.

Samples A through D solidified under four different cooling rates as a result of both different atomization gas pressures and powder sizes. The cooling rate for each case can be computed using well-established correlations.^[4] The cooling rates (K s^{-1}) of samples A through D are shown in Table I, computed as weighted averages for the powder sizes considered. The exact powder size corresponding to each cooling rate is shown in parentheses. The cooling rates for samples E and F were calculated from the heat extracted during deposition using a finite differences formulation^[3] and are also shown in Table I.

In solidification processes, the so-called cooling rate dT (K s^{-1}) is the product of the solid phase growth front velocity V_s (cm s^{-1}) and the thermal gradient ∇T (K cm^{-1}) across the solidification front (interface). The solidification front velocity, V_s , is a function of the amount of supercooling, ΔT , reached prior to solidification. An experimental cooling curve for an Al-6.9 wt pct Mn alloy has shown that at $dT = 3 \times 10^5 \text{ K s}^{-1}$, the supercooling is 329 °C below the melting point.^[5] As the rate of cooling increases, so does the supercooling. Similar relations were found for other alloys.^[5]

The microstructural evolution during solidification is strongly affected by the growth conditions at the solid/liquid interface. The extent of second-phase precipitation in a binary or ternary alloy system, for example, depends upon the amount of melt supercooling prior to solidification.^[6] The high heat extraction capability of rapid quenching processes enables large melt supercooling, high solidification front velocities, and steep thermal gradients across the propagating solidification interface. When a rapid growth rate is achieved in a binary system, the solute can be trapped into the freezing solid at composition levels higher than the equilibrium value for the corresponding liquid at the interface. In this case, as a result of the interface growing at a high rate and under large supercoolings, the chemical potentials of the components across the interface are not equal, as they should be for conditions of thermodynamic equilibrium, *i.e.*, for free energy minimization. For crystallization to occur at this stage, an increase in chemical potential of the solute across the interface must be balanced by a decrease in chemical potential of the solvent. Such a decrease, necessary for solidification, occurs only if the interface temperature has decreased significantly below the liquidus temperature. At the limit, partitionless solidification may occur, *i.e.*, the composition of the solid equals the composition of the liquid at the interface. The highest interface temperature at which partitionless solidification may occur is the temperature T_0 where the molar free energies of the liquid and solid phases are equal for a given composition. The locus of all T_0 temperatures over the whole range of compositions is the T_0 curve. This curve lies between the liquidus and solidus. The steepness of the T_0 curve is an indication whether or not a bound exists for the extension of solid solubility by rapid quenching.^[6,7] If the curve plunges to very low temperatures, single-phase (α or β) crystals with compositions beyond their respective T_0 curves cannot be formed from the melt. The best candidates for wide solid solubility extension are systems where T_0 curves are only slightly depressed; Al-Mn is such a system.

Table I. Solubility Extension (Weight Percent) of Mn in Al, Relative Amounts (Volume Percent) of MnAl Phases, and Computed Cooling Rates ($K s^{-1}$) (for Representative Powder Particle Sizes)

	Wt Pct Mn (by X-Ray) [†]	Wt Pct Mn (by EDAX)*	Cooling Rate [$K s^{-1}$]	Vol Pct MnAl ₆ (X-Ray)	Vol Pct MnAl ₄ (X-Ray)
Sample A (powder, 40 μm):	6.10 \pm 0.20	6.00 \pm 0.15	15.2 $\times 10^4$	nd**	0.45
Sample B (powder, 140 μm):	4.40 \pm 0.15	4.25 \pm 0.25	1.2 $\times 10^4$	3.20	0.40
Sample C (powder, 44 μm):	5.60 \pm 0.20	5.40 \pm 0.20	7.8 $\times 10^4$	nd	0.45
Sample D (powder, 140 μm):	2.10 \pm 0.10	2.15 \pm 0.25	0.98 $\times 10^4$	4.00	0.25
Sample E (spray deposit):	2.20 \pm 0.10	1.90 \pm 0.20	see text	3.60	0.40
Sample F (spray deposit):	2.25 \pm 0.10	1.95 \pm 0.10	see text	3.45	0.80

*Errors are standard deviations.

**nd = not detected.

[†]Estimated errors.

The Al-rich end of the equilibrium phase diagram for the Al-Mn system is shown in Figure 2. The eutectic temperature is 658.5 °C; the eutectic composition corresponds to 1.95 wt pct Mn. The solid solubility of Mn in Al decreases from 1.82 wt pct at the eutectic temperature to 0.36 wt pct Mn at 500 °C. The hypoeutectoid liquidus is a straight line intersecting the eutectic horizontal slightly below 2 pct Mn^[8] and coinciding with the solidus line and, therefore, the T_0 curve as well. Hence, the depression of the T_0 curve is very mild. The T_0 is then the extrapolated common liquidus-solidus line across the MnAl₆ + solid solution region, up to the composition limit of MnAl₆ (25.25 wt pct Mn). This is the maximum Mn solubility extension theoretically possible in Al. The T_0 curve has a nearly linear negative slope of 1.1 °C per wt pct Mn. A peritectic reaction takes place at 705 °C (710 °C in Reference 8) and 4.06 wt pct Mn, yielding two solid phases from the liquid, MnAl₆ and MnAl₄ (33.72 wt pct Mn).^[9] Supercooling causes the Al-Mn melt to reach temperatures well below T_0 , favoring extension of the solid solubility. If an Al liquid containing more than 4.06 wt pct Mn is rapidly quenched, both MnAl₆ and MnAl₄ can be present in the solid, as well as an extended solid solution of Mn in Al. Indeed, continuous increases of supercooling with increasing cooling rates for Al-Mn alloys showing extended solid solubility have been reported.^[9,10] Therefore, we can assume that the amount of solid solubility extension in Al-Mn alloys is related to the cooling rates experienced during processing.

In atomization, powders lose heat primarily by convection to the atomizing gas. An effective heat-transfer coefficient is achieved through high relative velocities between the gas and the powders, large surface to volume ratios associated with small diameter powders, and high thermal diffusivity of the atomizing gas.

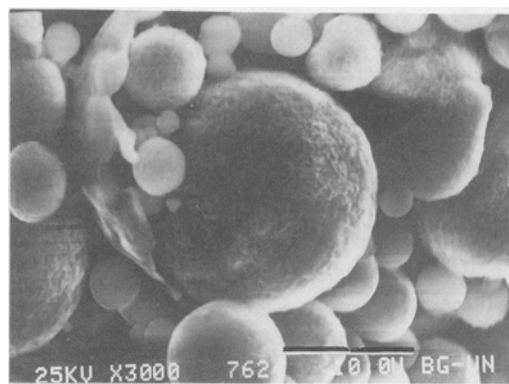
Assessment of the cooling rate during spray atomization and deposition is complicated by the variations in thermal environment prior to and after impact. At the moment of impact with the quenching substrate, a large proportion of the powders are still in the mushy state. A substantial part of the heat is extracted during cooling and solidification in flight during the atomization stage. The remaining enthalpy is dissipated during the deposition stage and transmitted to the substrate. In the course of the ongoing deposition, the bottom part of the deposit is quenched by the water-cooled copper substrate, while the upper part of the deposit is quenched by the depos-

ited material as well as by the impinging atomization gas. Therefore, the top and bottom regions of the spray-deposited materials experience different thermal histories. Recently, a mathematical model has been used^[11] to calculate droplet size distributions, droplet velocities, positions, temperature, cooling rates, and secondary dendrite arm-spacings during high pressure inert gas atomization and spray deposition. The results of that model suggest that at the moment of impact (in spray deposition), the droplet distribution still contains 15 to 30 pct liquid fraction by weight. The computed cooling rates after deposition and impact are approximately 10 to 20 $K s^{-1}$, well below cooling rates achieved during rapid quenching. The deposits, however, do exhibit microstructures characteristic of rapid solidification processing. This implies that the microstructure evolution in spray-deposited materials depends on the solidification conditions prior to impact rather than upon the heat transfer to the cooling substrate.

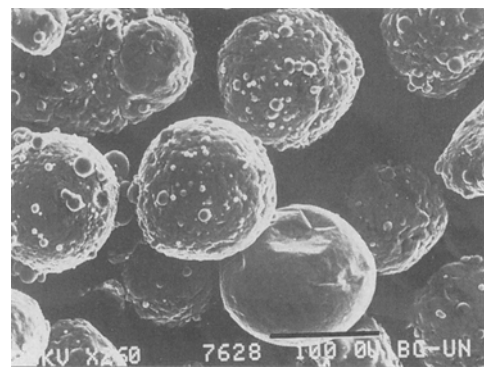
The effective cooling rates to be considered for spray-deposited specimens may be evaluated experimentally and then compared to those computed mathematically. This can be accomplished by evaluating the relative amounts of solid solubility extension of specimens that have been exposed to different cooling rates in both gas atomization and spray deposition.

In the present study, estimation of the amount of Mn in solid solution in the Al matrix was done by computing the lattice parameter change of Al (by X-ray diffraction, using $CuK\alpha$ radiation) through the dependence of the (331) Al interplanar spacing, d_{331} , on the Mn content,^[12] taking into account the presence of 0.65 wt pct Zr in the alloy. In addition, the amount of Mn in the Al matrix has been measured by energy dispersive analysis of X-rays (EDAX) in a 20 kV scanning electron microscope (SEM), using a spot size of 100 nm and a 30 deg tilt, with reference to pure Al and Mn as standards. The results are shown in Table I. The error evaluation is based on the standard deviations of the measured compositions and on the accuracy of the angle measurements in the diffraction results together with errors estimated by Ohashi *et al.*^[12] for d_{331} spacings interpolated for composition of 0.65 wt pct Zr in solution in the alloy.

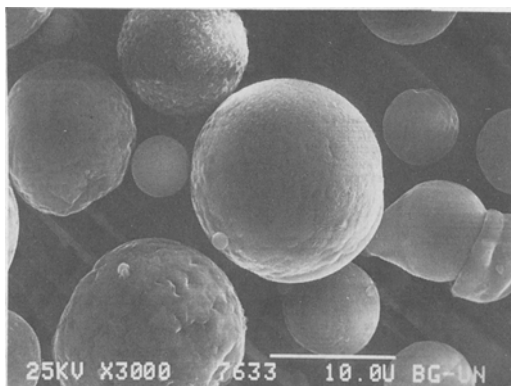
The X-ray experiments did provide useful information, not only on the lattice parameter changes from specimen to specimen, but also on the relative amount of secondary Mn phases, MnAl₄ and MnAl₆. The volume fractions of these phases have been determined by



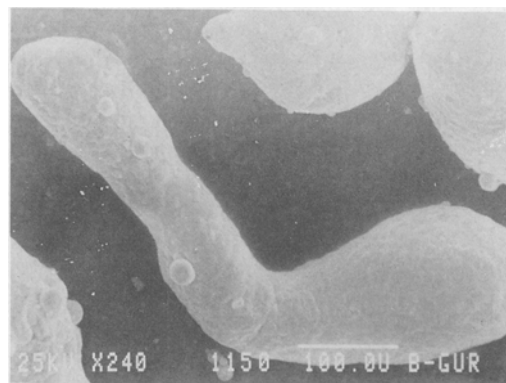
(a)



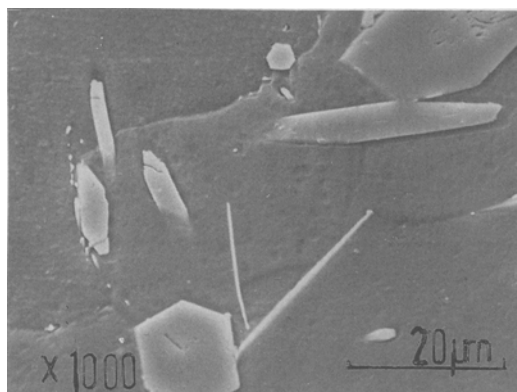
(b)



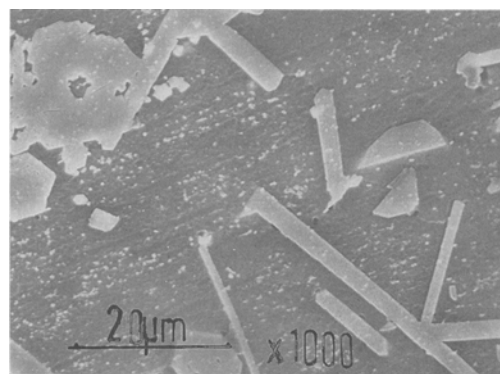
(c)



(d)



(e)



(f)

Fig. 2—The Al-rich side of the Al-Mn equilibrium phase diagram.

using the method of direct comparison^[13] and are shown in Table I. In sample A, the only Mn phase detected is MnAl_4 , in an amount of about 0.45 wt pct in volume fraction, accounting for the 0.5 wt pct Mn not in solution in the Al matrix. In sample C, the same volume fraction of MnAl_4 (equivalent to 0.50 wt pct Mn) is still present. No MnAl_6 has been detected in that sample, but there is evidence of an additional phase having an apparent fivefold symmetrical morphology in the micrographs of this specimen with apparent composition (as shown by EDAX) of MnAl_9 . This may account for the Mn balance (about 0.40 wt pct Mn unaccounted for). The fivefold symmetry phase is discussed elsewhere.^[14]

In sample B, the Mn phases detected are MnAl_6 (about 3.20 vol pct), MnAl_4 (about 0.40 vol pct), and the fivefold symmetry phase MnAl_9 (accounting probably for the 1.35 wt pct Mn missing for balance). In samples D through F, there is no indication of the fivefold symmetry phase, but the two other AlMn phases are present.

As seen in Table I, there is a clear correlation between the extension of Mn solid solubility in Al and the cooling rate experienced during the solidification process. Sample D, however, seems to show some discrepancy from the general trend. It should be recalled that this sample consisted of flat, elongated powders rather than spherical ones. The final solidification stage of these

powders (sample D) was not completed in flight but during impact on the atomization chamber walls (stainless steel). Since heat extraction by conduction into the chamber walls will be substantially lower than convective heat extraction during flight, the overall effective cooling rate of sample D powders was probably much lower than that calculated, as can be seen from Figure 3. This figure shows an exponential curve fit for the correlation between cooling rates and wt pct Mn in solid solution (as derived from lattice parameter changes) in samples A through C. For an effective, in flight cooling rate of $0.98 \times 10^4 \text{ K s}^{-1}$, as calculated for sample D, the extent of Mn solid solubility in Al should have been 4.25 wt pct (as computed from the curve fit equation). In fact, it is only $2.10 \pm 0.10 \text{ wt pct}$, as derived from the change in lattice parameter, or $2.15 \pm 0.25 \text{ wt pct}$, as measured by EDAX. This discrepancy can be attributed to the fact that a part, at least, of the solidification did take place during impact on the atomization chamber walls and, hence, at a slower cooling rate. This is consistent with the flat, elongated morphology of the sample.

The correlation shown in Figure 3 permits an estimation of the cooling rates experienced by the spray-deposited samples E and F. The lattice parameter changes for these two samples revealed a Mn content of 2.20 wt pct in sample E and 2.25 wt pct in sample F. The respective EDAX analyses showed 1.90 and 1.95 wt pct. The overall correlation between computed and measured extensions of Mn solid solubility in Al is fairly good. Therefore, it may be deduced that the effective cooling rates for spray deposition and for sample D are roughly

the same, i.e., at least $5 \times 10^2 \text{ K s}^{-1}$ for samples F and E. This has to be compared to the 10 to 20 K s^{-1} cooling rate experienced by the material after deposition.^[11] This implies that in spray deposition, solidification takes place partially in flight and partially during deposition. The microstructural changes during spray atomization and deposition should then be understood by considering the heat balance and solidification conditions controlling two distinct but closely linked stages: atomization and deposition.^[15] The final microstructure of the spray-deposited material will result from these complex quenching conditions.

The experimental work has been done at the Rapid Solidification Processing Laboratory, Materials Engineering Department, Ben-Gurion University, in partial fulfillment of MR's MSc. degree. E.J.L. wishes to acknowledge the Army Research Office (Grant No. DAAL03-89-K-0027) and the National Science Foundation (Grant No. MSS 8957 449) for their financial support. JCB gratefully acknowledges the support of a Grant-in-Aid (No. 3292/84) by the U.S.-Israel Binational Scientific Fund.

REFERENCES

1. J. Baram: *Mater. Sci. Eng.*, 1988, vol. 98, pp. 65-69.
2. E.J. Lavernia and N.J. Grant: *Int. J. Rapid Sol.*, 1986, vol. 2, pp. 93-106.
3. E. Gutierrez-Miravete, E.J. Lavernia, G. Trapaga, J. Szekely, and N.J. Grant: *Metall. Trans. A*, 1989, vol. 20A, pp. 71-85.
4. E.J. Lavernia and J. Baram: *J. Mater. Sci. Lett.*, 1988, vol. 8, pp. 612-14.
5. I.S. Miroshnichenko and G.P. Brekhayra: *Fiz. Met. Metalloved.*, 1970, vol. 29, pp. 664-66.
6. W.J. Boettinger and J.H. Perepezko: in *Proc. Symp. on Rapidly Solidified Crystalline Alloys*, Northeast Meeting of TMS-AIME, Morrison, NJ, May 2-3, 1985.
7. J.H. Perepezko and D.U. Furrer: *J. Appl. Phys.*, 1960, vol. 31, pp. 1136-37.
8. E.H. Dix, W.L. Fink, and L.A. Willey: *Trans. Am. Inst. Min. Metall. Eng.*, 1933, vol. 104, pp. 335-52.
9. R. Ichikawa, T. Ohashi, and T. Ikeda: *Trans. Jpn. Inst. Met.*, 1971, vol. 12, pp. 280-84.
10. I.S. Miroshnichenko and G.P. Brekhayra: *Phys. Met. Metalogr.*, 1970, vol. 29, pp. 244-34.
11. E.J. Lavernia and N.J. Grant: *Mater. Sci. Eng.*, 1988, vol. 98, pp. 381-94.
12. T. Ohashi, L. Dai, and N. Fukatsu: *Metall. Trans. A*, 1986, vol. 17A, pp. 799-806.
13. J.A. Sarreal and G.J. Abbaschian: *Metall. Trans. A*, 1986, vol. 17A, pp. 2063-73.
14. M. Ruhr and J. Baram: work in progress.
15. E.J. Lavernia: *Int. J. Rapid Sol.*, 1989, vol. 5, pp. 47-85.

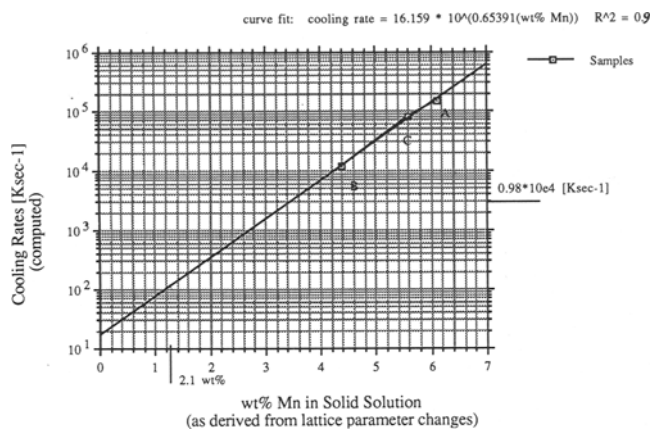


Fig. 3—Correlation between computed cooling rates and the extent of Mn solid solubility in Al (in wt pct Mn, as derived from lattice parameter changes).